Title	The nature of silicon nanowire roughness and thermal conductivity suppression by phonon scattering mechanisms
Authors	Glynn, Colm;Jones, Kim-Marie;Mogili, Vishnu;McSweeney, William;O'Dwyer, Colm
Publication date	2017-01-10
Original Citation	Glynn, C., Jones, K.-M., Mogili, V., McSweeney, W. and O'Dwyer, C. (2017) 'The Nature of Silicon Nanowire Roughness and Thermal Conductivity Suppression by Phonon Scattering Mechanisms', ECS Journal of Solid State Science and Technology, 6(3), pp. N3029-N3035. doi:10.1149/2.0071703jss
Type of publication	Article (peer-reviewed)
Link to publisher's version	10.1149/2.0071703jss
Rights	© The Author(s) 2017. Published by ECS. This is an open access article distributed under the terms of the Creative Commons Attribution Non-Commercial No Derivatives 4.0 License (CC BY-NC-ND, http://creativecommons.org/licenses/by-nc-nd/4.0/), which permits non-commercial reuse, distribution, and reproduction in any medium, provided the original work is not changed in any way and is properly cited. For permission for commercial reuse, please email: oa@electrochem.org. [DOI: 10.1149/2.0071703jss] All rights reserved. - https://creativecommons.org/licenses/by-nc-nd/4.0/
Download date	2023-05-04 20:08:41
Item downloaded from	http://hdl.handle.net/10468/3504

University College Cork, Ireland
Coláiste na hOllscoile Corcaigh

JSS Focus Issue on Thermoelectric Materials & Devices

The Nature of Silicon Nanowire Roughness and Thermal Conductivity Suppression by Phonon Scattering Mechanisms

Colm Glynn,[a] Kim-Marie Jones,[b] Vishnu Mogili,[c] William McSweeney,[a] and Colm O'Dwyer[a,d,*,z]

[a]*Department of Chemistry, University College Cork, Cork T12 YN60, Ireland*
[b]*Department of Physics and Energy, University of Limerick, Limerick, Ireland*
[c]*Centro Nacional de Pesquisa em Energia e Materiais (CNPEM), Brazilian Nanotechnology National Laboratory (LNNano), CEP 13083-970 Campinas/SP, Brazil*
[d]*Micro-Nano Systems Centre, Tyndall National Institute, Lee Maltings, Cork T12 R5CP, Ireland*

The nature of the surface roughness of electrolessly etched p-type Si nanowires (NWs) is examined using high resolution transmission electron microscopy and shown to comprise individual silicon nanocrystallites throughout the waviness of the roughness features. As the frequency of roughness features are believed to be sources of surface and boundary scattering, the thermal conductivity below the Casimir limit is still not fully explained. The frequency shift and development of asymmetry in the optical phonon mode in silicon was monitored by Raman scattering measurements as a function of temperature (>1000 K). We assessed the influence of Si NW roughness features on phonon scattering mechanisms including quantum confinement of phonons from roughness nanocrystals, boundary scattering, and optical phonon decay to interacting 3- and 4-phonon processes that may contribute to the cause of significant thermal conductivity suppression in rough Si nanowires. High temperature studies and detailed examination of the substrate of roughness revealed high frequency optical phonon contributions to thermal conductivity suppression.

Manuscript submitted November 7, 2016; revised manuscript received December 27, 2016. Published January 10, 2017. *This paper is part of the JSS Focus Issue on Thermoelectric Materials & Devices: Phonon Engineering, Advanced Materials and Thermal Transport.*

In order to realize increasingly efficient thermoelectric materials and devices, various methods have been employed to reduce or interfere with phonon propagation and heat conduction.[1–6] This may involve the addition of impurities, modification of crystal structure,[7] or more complex alloy formation to scatter phonons to lower the thermal conductivity and diffusivity.[8] Nanowire (NW) structures with reduced dimension also show promise in affecting heat transport.[9,10] Phonon scattering at the material boundaries (surfaces, grains etc.) is useful since the bulk of the material and so the electronic conductivity is in principle unaltered, unlike some alloying and impurity scattering approaches.[11,12] Thus, promising values of $ZT = S^2\sigma T/\kappa$ are now commonplace, and approaching unity for silicon. Here, S is the Seebeck coefficient, σ is the electrical conductivity, T is the absolute temperature, and κ is the thermal conductivity comprising electronic (κ_e) and lattice (κ_l) contributions.

Roughened Si NWs produced by electroless etching of Si wafers exhibited severely suppressed thermal conductivity as low as 1.6 W m^{-1} K^{-1} for a 56 nm diameter NW at 300 K.[2] That work used etched vapor-liquid-solid (VLS)-grown NWs and are not definitively p-type or n-type, and so the electronic contribution to thermal conductivity is less-defined, although for values $<10^{19}$ cm^{-3} (electron mean-free path $\sim$10 nm),[13] it is not likely to be dominant over lattice thermal conductivity where the heat in silicon is transported by phonons with mean-free paths $>$ 200 nm. That report of such a low thermal conductivity, even accounting for diffused phonon boundary scattering, is below the Casimir limit[14] and remains as yet not fully explained.[15,16] At the core of the debate is the nature of the roughness and several factors are important here: 1) does the rms roughness value matter, 2) are certain bandwidths of phonon wavelengths strongly contributing to enhanced scattering, 3) does phonon backscattering occur, 4) is the roughness composed of sub-structure not previously identified, 5) does phonon confinement occur and what are the optical and acoustic phonon mean free paths, and 6) what type of boundary scattering occurs and what length scales of Si features really contribute in the absence of impurity scattering.

There are many theories that attempt to explain the significant reduction in thermal conductivity.[17–19] Separately, there are many useful investigations of NW and nanoscale Si Raman spectra, citing the influence of size, doping type, carrier concentration,[20] crystallographic orientation and heating on the optical phonon modes[21,21] – these analyses can be reassessed to provide useful characterization of the roughness characteristics that influence phonon transport in Si NWs. Despite recent advancements to quantify the surface roughness and its relationship to thermal conductivity reduction, there is still a lack of information on the atomic scale and nanocrystalline structure of the roughness features and its interface with the solid NW core.[23] Radiative and convection issues have limited most studies of thermoelectric rough Si NWs to room temperature or lower, and high frequency optical modes may carry a significant fraction of heat at elevated temperatures in silicon, with Umklapp or multiphonon processes also possible.

Here, we show that MAC-etched Si NWs directly from p-type Si forms layers of NWs whose roughness is more complex than forming a random, seemingly correlated roughness with a band of roughness wavelengths – the rough features contain individual crystallites that confine optical phonons and scatter acoustic phonons, and regions of the polycrystalline roughness have grain boundaries that are $\sim$2–5 nm apart, providing a basis for scattering mechanisms that were not previously considered in the roughness.[24] We determine the change in LO phonon mode as a function of direct heating of the NW arrays and characterize the LO mode structure to show that phonon confinement, scattering mechanisms and thermal conductivity is affected by the unique polycrystallinity of the roughness and that the optical phonon shifts and asymmetry can trace the reduction in phonon transport.

*Electrochemical Society Member.
[z]E-mail: c.odwyer@ucc.ie

Experimental

The Si NWs were fabricated by metal-assisted chemical etching of a bulk single-crystal p-type B-doped 200 mm diameter Si(100) wafer (680 μm thickness) with a native oxide layer (~2–5 nm thick). The p-Si(100) had a nominal resistivity of 1–30 Ω · cm corresponding to an electronic carrier concentration in the range 1.6–7.0 × 10^{14} cm^{-3}. Each wafer was cut to a size of 5 mm × 10 mm and then cleaned using iso-propyl-alcohol (IPA) before etching. Wafer coupons were sonicated for two cycles in IPA for 20 mins at 40°C and dried under nitrogen flow. Substrates were immersed for 2 h in a heated solution of 10% HF containing 0.04 M $AgNO_3$ and maintained at 50°C using a thermostated water bath. We should point out that most of the primary reports on rough NWs as thermoelectric materials have been MAC-etched vapor-liquid-solid (VLS) grown NWs, and so are intrinsically doped.[25–28] In our case, we create a layer of NWs directly from a Si(100) wafer coupon.

Raman scattering was acquired using a Horiba Jobin Yvon Dilor XY Labram spectrometer with an Olympus BX40 confocal microscope. Optical excitation was provided by a 532 nm solid state 100 mW laser and a 633 nm 20 mW laser and spectra were collected with a Peltier-cooled CCD detector. Comparative spectra collected under 785 nm excitation was acquired using a Renishaw InVia Raman spectrometer with a RenCam CCD camera. Scanning electron microscopy (SEM) of cleaved (011) cross-sections and (001) plan view of the Si NWs were examined on a Hitachi S4800 FESEM operating at 5 kV. TEM was conducted at 200 kV using a JEOL TEM JEM-2100F. For STEM analysis, the E-beam spot size was 1.5 nm with a camera length of 40 cm using a condenser aperture of 100 μm.

Angle-resolved optical characterization was conducted using an in-house cage-mounted optical reflectance/transmission spectroscopy setup. White-light broadband illuminated was provided by a collimated halogen bulb. UV-Vis-NIR spectra were acquired using an Oceanoptics USB2000+ and a NIRQuest256-2.5, with optical resolutions of 1.5 nm and 9.5 nm respectively, referenced to a Au mirror (ThorLabs gold mirror PF10-03-M01) standard.

Stage heating for uniform thermal equilibration prior to Raman excitation was carried out using a Linkam TS1500 Heating Stage with associated power supply unit, controlled pumped water cooling to maintain a constant temperature, and a TMS 94 temperature controller. The temperature controller was programmed to heat the sample in increments of 50 K at a rate of 35 K min^{-1} in an enclosed ambient air environment. The sample was generally heated to 1173 K and then the sample was cooled in increments of 50 K at the same rate. The temperature was held at each increment for 3 mins and two spectra were obtained for that temperature.

Relevant phonon scattering and confinement concepts.—In this section, we summarize salient models of phonon confinement and scattering, caused by reduced dimension and surface scattering primarily. These properties are by no means exhaustive, and the reader is referred to excellent reviews on various formalisms for phonon transport and physics.[29] These models however, are amenable to probing by Raman scattering to gauge the effect of micro- and nanostructure on optical phonon modes.[22,30–32] The recent advances made in assessing roughness and phonon scattering physics that cause thermal conductivity reduction below the Casimir limit can be found in the references.

The Micro Crystal Model (MCM) and the quantum confinement effect are used to explain optical properties of many nanoscale structures, specifically for longer mean free path optical phonons rather than acoustic phonons. According to the MCM, the theoretical first-order Raman spectrum can be obtained from the following relation[33]

$$I(\omega) = \int \frac{d^3 q C(0,q)^2}{[\omega - \omega(q)]^2 + \left(\frac{\Gamma_0}{2}\right)^2} \quad [1]$$

where $\omega(q)$ is the phonon dispersion curve (q, the phonon wave vector); Γ_0 is the natural linewidth (inversely proportional to the intrinsic phonon lifetime); C(0,q) is the coefficient describing the phonon confinement at $q_0 = 0$, which is appropriate for first-order Raman scattering. The integration must be performed over the entire Brillouin zone, which is a uniquely defined primitive cell in reciprocal space. The confinement function is typically Gaussian and follows

$$|C(0,q)|^2 = \exp\left(\frac{-q^2 L^2}{16\pi^2}\right) \quad [2]$$

where L is a parameter describing the grain size with a unit of a, where a is the lattice constant of single crystalline silicon. The predicted shift and change in the LO phonon for example, did not follow this model at higher temperatures, and effects of impurity scattering, doping and the nature of the structure of nanoscale Si that affects overall phonon scattering or confinement resulted in greater (optical phonon) mode shifts.[21,34] Confinement of the spatial wave function of the optical phonon modes in nanostructures such as Si NWs, is accompanied by a relaxation of the momentum conservation laws.[35] The Raman scattering is therefore no longer confined to the center of the Brillouin zone, where $q = 0$. Most of the phonons with a non-zero q are activated. This model is limited and most sensitively quantifies the effect of size and spatial phonon confinement on the linewidth of the optical phonon.

To probe the effect of temperature, Balkanski et al.[30] proposed that both the line-width and frequency of the optical modes of vibration within Si vary with temperature. They analyzed the cubic and quartic contributions of the LO phonon from the Raman spectrum of bulk Si, the damping constant of this phonon, and also the temperature dependence of the frequency shift – anharmonic terms were required to effectively model the thermalized phonon modes, particularly when the temperature dependence of the thermal conductivity is known. Briefly, temperature-induced mode shifts of the optical phonons arise from anharmonic terms in the vibrational potential energy, whereby optical phonons exchange energy with other modes in the lattice in order to achieve thermal equilibrium – the optical phonon can be considered as three or indeed four interacting acoustic phonons.

The simplified model follows:

$$\omega(T) = \omega_0 + C\left(1 + \frac{2}{e^x - 1}\right) + D\left(1 + \frac{3}{e^y - 1} + \frac{3}{(e^y - 1)^2}\right)$$

$$\Gamma(T) = A\left(1 + \frac{2}{e^x - 1}\right) + B\left(1 + \frac{3}{e^y - 1} + \frac{3}{(e^y - 1)^2}\right)$$

$$x = \frac{\hbar\omega_{0_{(T=0)}}}{2k_B T}; y = \frac{\hbar\omega_{0_{(T=0)}}}{3k_B T} \quad [3]$$

where ω(T) is the Raman shift and Γ(T) is the linewidth shift, both caused by temperature and $\omega_{0_{(T=0)}}$ is the frequency of the optical phonon at a temperature of 0 K. A, B, C, D and ω_0 are fitting constants, which are calculated for each separate data series. At temperatures above 600 K, the inclusion of four phonon processes is required to accurately predict the phonon transport behavior of silicon. The model has since been modified to account for the experimental observations of Si NW Raman scattering. Terms are introduced to the model to account for both the temperature effects and the stress effects caused by the heating of the Si NWs. Chen et al.[36] put forward a modification where these two terms can be combined together to give:

$$\Gamma(T) = A\left(1 + \frac{2}{e^x - 1}\right) + B\left(1 + \frac{3}{e^y - 1} + \frac{3}{(e^y - 1)^2}\right) + \Gamma_1 \quad [4]$$

where Γ_1 is the new term due to spatial confinement effect, which takes the additional broadening of the LO mode into account. The shifting of the LO mode toward lower wavenumbers, as well as the broadening of the mode, is indicative of the phonon anharmonicity. However, for each separate nanoscale Si, it has been difficult to accurately determine the FWHM broadening. The frequency of the LO phonon can be obtained from:

$$\omega(T) = \omega_0 + \Delta_{TE}(T) + \Delta_A(T) \quad [5]$$

where ω_0 is the frequency at absolute zero, $\Delta T_{TE}(T)$ is the shift of the LO mode caused by thermal expansion and $\Delta T_A(T)$ is the shift of the LO mode caused by the anharmonic phonon-phonon coupling.[12]

Both the 3 or 4-phonon anharmonic process model for temperature dependence, and the MCM model to account for size or confinement effects, largely describe the salient features of simple NW structures, as mapped in optical phonon modes under excitation via Raman scattering[20] – however, many forms of NWs are much more complex and size effects with temperature variation require additional considerations, including crystallinity, morphology, electronic carrier concentration, Umklapp processes, surface and boundary scattering and several other phenomena.[37] Hao recently developed a model that can be adapted to probe the influence of grain size variation, internal grain substructure, interface boundary scattering and phonon transport on polycrystalline components.[38]

When the average size of the nanocrystallites is less than the phonon mean free path of monocrystalline Si at room temperature (Λ_{Si}), phonons scatter on the boundaries of the crystallites predominantly, not within the crystallites. Therefore, the temperature gradient and thermal conductivity are often defined on the boundaries and the phonon transport between two opposite boundaries is considered ballistic. Underlying these effects, is the nature of the true Si NW morphology – of what is the roughness comprised? Are nanocrystallites uniquely sized and distributed? Is the NW diameter contributory, when the walls are rough or the NW is internally porous? Are there scaling laws to capture a description of roughness that avoids the randomness of different NWs, that can be definitively used to assess relative thermal conductivity by understanding phonon scattering from all contributory processes?

One recent model that directly tackles the nature of surface boundary scattering in NWs with rough surfaces, that show significant reduction in thermal conductivity, has focused on understanding the frequency dependence of the roughness.[39] This model was developed after it was realized that rough NWs reduce thermal conductivity to values much lower than the Casimir limit, implying mechanisms additional to dominant surface boundary scattering. Even still, the nature of the roughness is unclear, and often inconsistent and a function of the etching method.

To briefly summarize the approach in Ref. 3 using the Born approximation employed by Martin et al.[15] in a separate paper, the frequency-dependent boundary scattering rate $\tau_{i,j}^{-1}(E)$ can be represented by a surface integral, $S(E')$, taken over the area of the surface of constant energy, E', as

$$\tau_{i,j}^{-1}(E) \propto \int_{E'} \frac{S(q = \mathbf{k} - \mathbf{k}')}{\nabla_{\mathbf{k}'} E'(\mathbf{k}')} dS(E') \quad [6]$$

which describes a phonon with wavevector $\mathbf{k}$ from branch i scattered to a phonon from branch j with wavevector $\mathbf{k}'$. $S(q) = S(\mathbf{k} - \mathbf{k}')$ is the Fourier transform of the spatial autocorrelation function i.e. the power spectrum of the rough NW surface. Accurately quantifying precisely what $S(q)$ comprises is critical to understand the processes that suppress thermal conductivity. Several recent approaches have assessed roughness in terms of a frequency or mode dependence and with correlation functions for random roughness features often used in surface metrology. The surface roughness can be obtained through the auto-covariance function $C(x) = \langle [z(x_0 + x) - \langle z \rangle][z(x_0) - \langle z \rangle] \rangle$, where $z(x_0)$ is the height at a point x_0, and x is the lateral separation between two surface points, formulated as $C(x) = \sigma^2 \exp[-(|x|/\xi)^{2h}]$, where σ is the rms roughness $\sigma_{rms} = \left[\frac{1}{N}\sum_{n=1}^{N}(x_n^2)\right]^{1/2}$ and ξ the lateral correlation length where x where the function decays to $1/e$.[24] Here, $\xi \propto L$, the correlation length that can be determined from Raman scattering spectra. Lim et al.[3] extended the analysis by obtaining a power law scaling instead of the typical Lorentzian profile describing the Fourier transform of the auto-covariance function. Their fitting to measured roughness profile of NWs proposed a power spectrum to capture all roughness wavelengths in the range 1–100 nm as the rms roughness was deemed to be the major contributor to phonon scattering compared to NW diameter as follows:

$$S(q) = \alpha\left(\frac{q_0}{q}\right)^n \quad [7]$$

where q comprises wavevectors of the roughness from 1−100 nm ($10^{-2} - 10^0$ nm^{-1} in this case) are considered. α and n are fit parameters, and $q_0 = 1/0.313$ nm was the inverse of the lattice constant of Si in the $\langle 111 \rangle$ direction. We assume the authors chose the $\{111\}$ planes as representative slow etch planes typically relieved when a (100) surface is etched – the actual roughness accommodates many more crystallographic directions. The exponent n is related to the nature of the roughness.

The approach improved upon roughness spectral analysis, but the method did not accurately capture the roughness spectrum at critical wavelengths, and successfully correlating the latter roughness parameter to the bandwidth of phonon wavelengths that cause scattering, was proposed. However, the nature of the roughness and what exactly causes scattering has remained elusive until now – rough features as we will show, have internal nanocrystallite content within the structure which is measured as part of the roughness 'wavelength'.

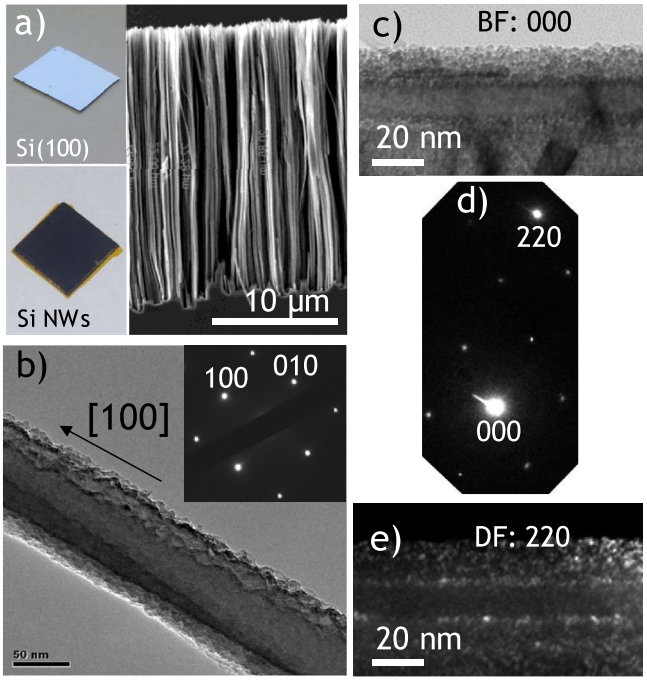

Figure 1. (a) Photographs of pre- and post-MAC etched Si(100) coupons. The Si NW layers exhibit broadband visible light scattering, and SEM image of the NW layer cross-section. (b) TEM image of single NW showing a roughened surface. The inset electron diffraction patter confirms a diamond cubic structure. (c) Bright field HRTEM image along the (010) zone axis of the nanowire outer surface showing characteristic roughness. (d) dual beam electron diffraction pattern from (c) and (e) the corresponding dark field HRTEM image from the (220) reflection of the NW showing individual Si nanocrystal content within the rough features.

Results and Discussion

Nanoscale substructure of Si NW roughness.—Figure 1a summarizes the NW array formation after metal-assited chemical etching. Each NW is formed with a roughened side wall (Fig. 1b) yet the core is always maintained and no sub-surface porosity is evident. The MAC process etches the entire bulk Si surface to relieve a black silicon-like coating of vertically aligned Si NWs with lengths in this case of 20–22 μm. High resolution TEM data in bright field (Fig. 1c) and dark field (Fig. 1e) confirms that the roughness comprises nanocrystalline features with a different orientation to the parent NW – the roughness,

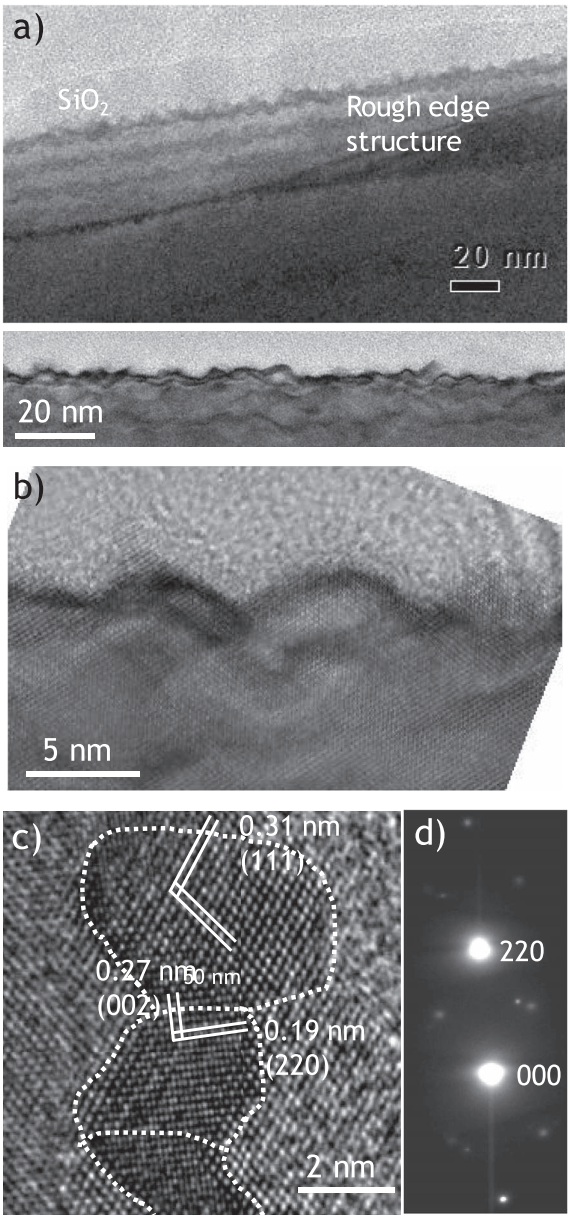

Figure 2. (a) TEM images of the roughness features on p-type MAC etched Si NWs. (b) HRTEM image of the atomically resolved lattice of a portion of the rough outer surface of a NW. (c) HRETM image confirming oriented grains of Si nanocrystallites comprising the roughness, also confirmed by dual-beam electron diffraction in (d). Lattice interplanar spacings are shown for two orientations of Si nanocrystalline grains of ∼2–3 nm in dimension.

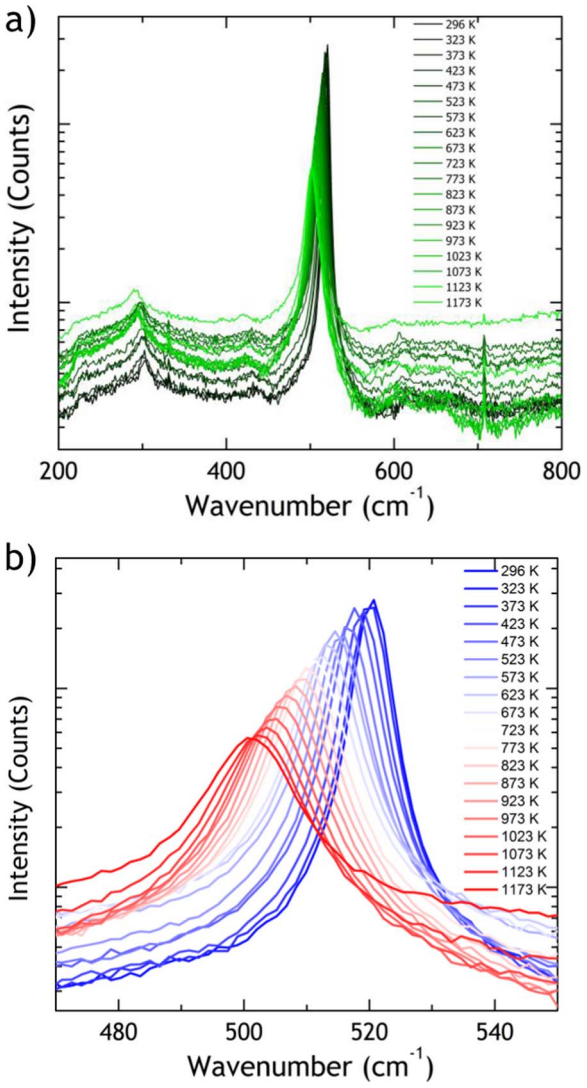

Figure 3. (a) Raman scattering spectra for p-Si NWs acquired after thermal equilibration to temperatures in the range 296–1173 K. (b) The Si NW LO phonon spectral broadening and shift as a function of temperature.

unlike MAC etched VLS NWs, is not only a random waviness of the as-made wall structure.

Figure 2a shows the nature of the surface roughness features in more detail. This waviness is somewhat different to the undercut and non-crystallographically relived faceting in MAC-etched VLS NWs.

Characteristically, as identified in previous work,[40] rough Si NWs formed by MAC etching retain a stoichiometric SiO_2 oxide coating due to the process of Si oxidation that facilitates etching in HF acid.[25] Interestingly, computational analysis of NW with amorphous silica coatings shows a 30-fold decrease in thermal conductivity compared to bulk silicon for 15 nm diameter NWs.[41] Experimentally, single NW or bundle/array measurements that use metallic contact-based method must avoid contact resistance effect in oxidized NWs, but spectroscopic approaches are promising in this regard for oxidized rough NWs. The degree of roughness is consistent at lower magnification, however in Fig. 2b, the atomic scale resolution images show individual nanocrystallites, and grains of Si with a different orientation to the image zone axis. Figure 2c shows that the diamond cubic structure of silicon is unchanged, yet grains within the roughness are caused by twisting and off-axis orientation of 2–5 nm segments, which are small enough to confine optical phonons, cause phonon scattering and affect acoustic phonon transport. Separate evidence of these crystallites within the roughness was obtained by photoluminescence, whereby light emission signatures matched those of Si nanocrystals.[40] STEM images use secondary electrons and the information avoids contributions from electron transparent sections of NW roughness features in projection, thus the nature of the roughness crystallinity is accurately representative.

Optical phonon scattering in rough Si NWs.—Figures 3a, 3b show the temperature-dependent Raman scattering spectra for the electrochemically roughened p-type Si NWs, acquired at low laser power density to avoid localized heating during equilibrated sample heating. The overall Raman spectrum for Si in Fig. 3a shows the classic response of a single crystal Si, with the dominant LO mode centered at ∼520 cm^{-1} and the 2TA phonon at ∼302 cm^{-1} at room temperature (296 K). All modes redshift with increasing temperature

and as shown in Fig. 3b, a significant asymmetric broadening of the LO mode occurs, with a corresponding reduction in mode peak intensity.

In Fig. 3a, it is clear that at each equilibrated temperature, the 2TA acoustic phonon modes do not become flat and thus resistive phonon-phonon processes that cause phonon mean-free path reduction do not seem to be caused by the rms roughness nor the nanocrystalline compnent of the roughness features.

The most extensively used model to determine an effective correlation length considers[42] the LO phonon mode shift and predicts a corresponding crystallite size according to:

$$\Delta\omega(\xi) = -A\frac{a_0}{\xi}\gamma \qquad [8]$$

where $\Delta\omega(\xi)$ is the shift in the TO mode of the nanocrystals, ξ is the correlation length (nm), a_0 is the radius constant of the Si crystal (nm) and A and γ are constants. The correlation length ξ estimated by this model is related to the average grain size in nanocrystalline materials or to the average distance between defects in crystals. The correlation length is related, but not identical, to the phonon mean free path but considers the phonon confinement effect and is less accurate for small (<3 nm) crystalline features that result in a significant asymmetry in the LO phonon mode shape.

The correlation length can be measured from the FWHM of the LO peak from the data in Fig. 3 using the following empirical relation, from Viera et al.:[22]

$$FWHM(\xi) = \frac{2\xi + 6.2618}{0.81004\xi - 1.6053} \qquad [9]$$

The FWHM and the correlation length are plotted in Fig. 4a as a function of temperature from 296–1723 K and also in reverse (cooling), directly from Raman spectral analysis. The correlation length decrease from 6 to 3 nm at 1723 K. We note that no irreversible modification to the structure or phonon mode shape is caused by heating. The mode shape is also important and in Fig. 4b, we show the coefficient of broadening, C_b. The increase can also be seen in the spectra in Fig. 3b. The trace matches the FWHM, implying a dominant low wavenumber modification of the mode line-shape, with a concomitant peak location decrease that is linear with the increase in FWHM (Fig. 4c). Suppressed thermal conductivity (see further below) is characteristic of asymmetric broadening of the LO mode and are consistent with both phonon confinement and multi-phonon processes as will be discussed next. Since the shift is too significant to account for optical phonon confinement only, and boundary scattering from within the roughness is likely a contributory factor. We note that these shifts do not contain dominant contributions from stress modification upon heating, which must occur simultaneously. Typically, in NW systems of Si and Ge, modal frequency decrease from tensile stress in the NW core (not outer nanocrystallites) are just several wavenumbers. Our measurements contradict those of Feser et al.,[39] at least in mode shift with FWHM, primarily since our etched features do contain crystallites that contribute to confinement, but thermal conductivity is reduced with mode broadening. Their NWs are electrolessly etched VLS NWs, and we assume that their NWs are devoid of internal stacking faults, grain boundaries or other defects and are of similar dimeter. By comparison to Eq. 5, we propose that anharmonic phonon-phonon coupling and multi-phonon processes play a significant role in the deviation of nanocrystalline roughness-containing solid NWs compared to bulk Si – the mode shift is dominated by the $\Delta_A(T)$ term which describes phonon-phonon anharmonic interactions.

To examine the contribution of optical phonon reducibility to acoustic phonons by cubic and quartic anharmonic interactions, we employed a modified multiphonon process model developed by Balkanski to our Raman data (Eq. 3) for the LO phonon temperature dependence, accommodating spatial confinement effects of nanocrystals in the roughness features. This contribution is well known for bulk silicon, but has not been applied in detail to rough Si NWs, particularly since the roughness parameters (correlation length, rms roughness) and their relation to the bandwidth of phonons that carry heat, has been a recent focus. In Fig. 5a, A, B, C, D, Γ_1 and ω_0 from Eq. 3 are

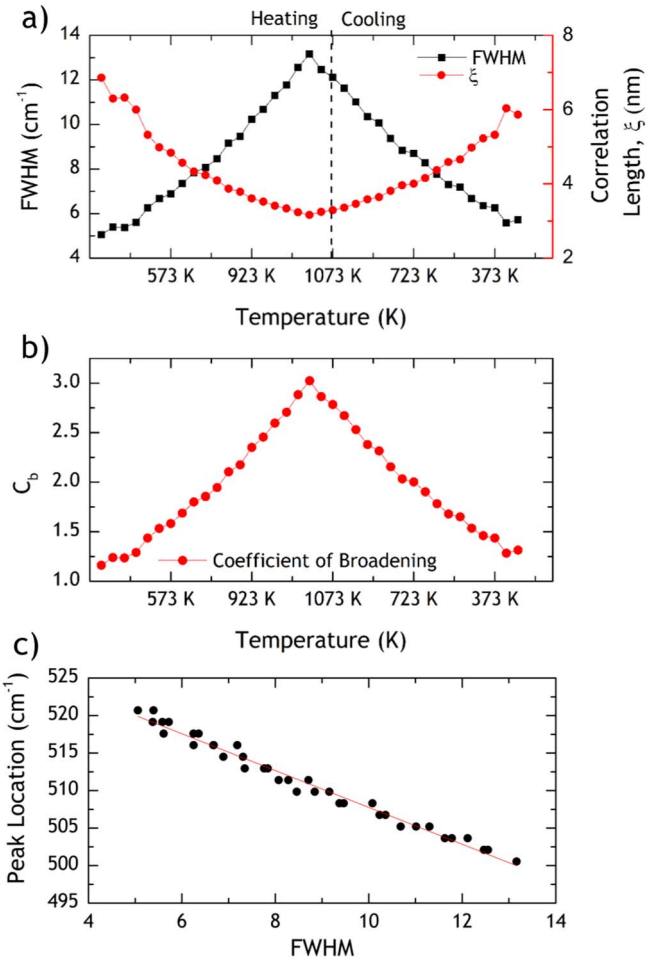

Figure 4. (a) Full Width at Half Maximum (FWHM) and correlation length associated with of the LO phonon mode from Raman scattering spectra for p-Si NWs acquired at temperatures in the range 296–1173 K (heating) and in reverse (cooling). (b) The coefficient of peak broadening as a function of temperature. (c) LO phonon mode peak wavenumber as a function of FHWM for both heating and cooling cycles.

fitting constants which were calculated for each data series, to model 4-phonon processes. Removing two anharmonic constants D and B allows a 3 phonon model to be calculated and compared.

Both the Raman shift and FWHM (Fig. 3a,b) vary with temperature and can be fitted very well by 3 phonon processes up to ~800 K and a similar trend is found for bulk Si. Above 800 K, the deviation requires 3 and 4-phonon processes to accurately fit the experimental data. The optical phonon mode shift is less dependent on a fourth phonon process at all temperatures. The FWHM requires an anharmonic 4 phonon process involving the decay of the initial optical phonon to others with lower group velocities. To accurately fit the data at all temperatures, for solid-core NW with nanocrystalline component in their surface roughness. Recently, Feng et al. determined through computational investigations[43] that anharmonic materials such as Si require fourth and higher order phonon processes to explain the thermal conductivity reduction at higher temperatures, in line with our experimental results for rough Si NWs. Their study concludes that even at low temperatures, optical phonon scattering also dominated by 4 phonon processes, and thus compared to experimental data provided here for rough Si NWs, 4 phonon scattering rates are significantly affected by the nanocrystalline grain-containing Si NW outer surface roughness.

Thermal conductivity from optical phonon scattering.—The thermal conductivity of bulk Si and Si NWs with nanocrystalline roughness features was estimated using the temperature increase caused by

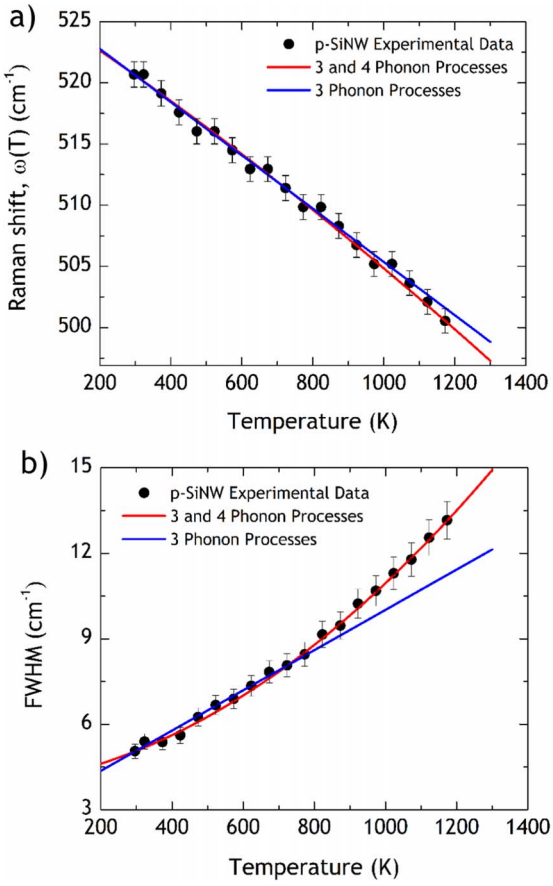

Figure 5. (a) LO phonon mode Raman shift as a function of temperature from Raman scattering data of rough p-Si NWs. Fits of 3- and 4-phonon processes according to Eq. 3 are overlaid. (b) FWHM of LO mode as a function of temperature and modelled fits of 3- and 4-phonon processes are overlaid. Error bars represent standard deviation of measurements from 3 separate spectra at each temperature.

a heated laser probe, assuming a semi-infinite effective medium with efficient optical absorption. This technique was adapted by Perichon et al.[44] to calculate the thermal conductivity of silicon using Raman spectroscopy. The thermal conductivity, κ, can be estimated using the linear relationship: $\kappa = 2P/\pi a \Delta T$, where P is the heating power of the incident laser, a is the diameter of the laser spot (2.6 μm) and ΔT is the change in temperature between two laser heating temperatures; these temperatures are usually the room temperature value and a higher local sample temperature. As the nanocrystallite features (d_c) within the roughness waves are considerably smaller than the phonon mean free path (Λ_{Si}), the effective thermal conductivity can be estimated according to $\kappa_{eff} = \frac{1}{3} c v \Lambda_{eff}$, where c is the specific heat per unit volume of the nanocrystallites, v is the mean sound velocity and Λ_{eff} is the effective mean free path of phonons given by

$$\Lambda_{eff} = \frac{\Lambda_{Si}}{1 + \frac{4\Lambda_{Si}}{3d_c}} \quad [10]$$

The temperature of the sample was estimated by comparing the thermal effect on the LO mode due to site-specific heating on the NW layer with a high laser power density, to that of uniform sample heating from a heating stage shown in Fig. 3. The temperature of the Si NWs was estimated by comparing the red-shifting of the LO mode for high laser powers to that found from uniform heating experiments at similar temperatures, shown earlier.

The thermal conductivity of the Si NWs was calculated using the same method, with the local temperature calculated using the Raman shift of the zone-center LO phonon. A laser power was chosen to ensure a comparable temperature to bulk Si(100) measurement as a comparator. At a laser power of 25 mW under 532 nm excitation, the LO mode shifted to a value of 513.8 cm^{-1}, corresponding to a local temperature of 600 K. Using the above values, the thermal conductivity of the Si NWs was calculated to be 18.71 W/mK. This value assumes 100% absorption of the incident energy. Visible frequency optical reflectance measurements (Fig. 6a) confirm <0.5% reflectance at 532 nm (and indeed across the entire broadband visible spectrum) for Si NW layer at an angle of incidence of 45° – all sample regions probed were vertically aligned NWs, connected to the substrate. By comparison, the absorptance of rough NWs was simulated by Hu et al.[45] and they predicted an absorptance of 68% for lightly p-doped Si NWs with a diameter of 80 nm. For the p-Si NWs studied, this is a reasonable approximation; a significant contributor to reflectance suppression (>99%) is due to extrinsic scattering of a dense array of NWs. This absorptance provides an effective thermal conductivity of 12.72 W/mK for the NW.

The clumping and disorder associated with the Si NWs can be regarded as a degree of porosity and important to consider when Raman scattering spectra are acquired from NW arrays after MAC-etching, as shown in a plan-view SEM image in Fig. 6b. It has been shown that the porosity of the sample affects the overall thermal conductivity:

$$\kappa = \kappa_{eff}(1 - P)^3 \quad [11]$$

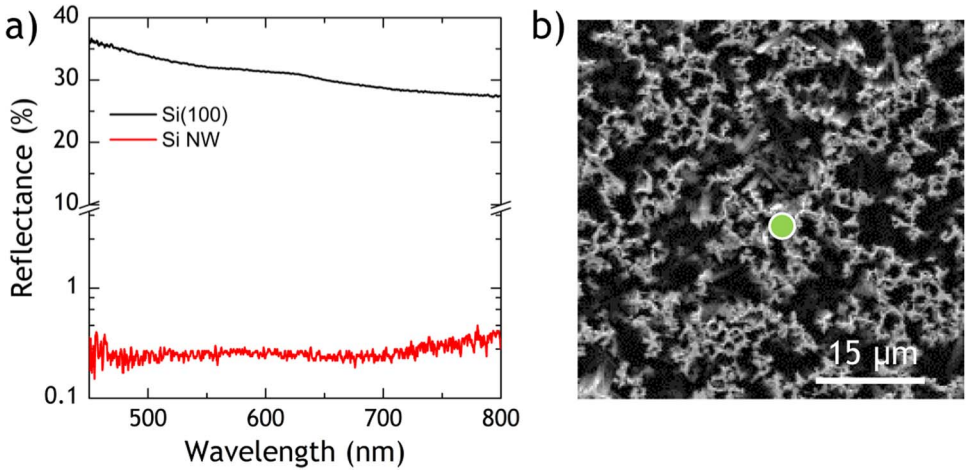

Figure 6. (a) Visible frequency range optical reflectance of Si(100) and a Si NW layer acquired at angle of incidence of 45°. (b) Plan-view SEM image of a MEC-etched Si NW layer with average laser spot beam waist overlaid.

where κ_{eff} is the thermal conductivity of the NWs, P is the porosity of the Si NW region under optical excitation, determined previously from plan view SEM micrographs on NW layers.[20] This form of porosity is distinctly different from the Eucken form ($\kappa_{pore} = \kappa_l \frac{(1-\emptyset)}{(1+\emptyset/2)}$), where κ_l is the lattice thermal conductivity, and $\emptyset$ is the volume fraction of pore *within* the NW, i.e. such as a mesoporous NW. Rough NW are non-porous and the lattice conductivity κ_l used in this calculation is the reduced value measured by Raman scattering. The porosity of the sample region containing Si NWs in the beam waist of the probe laser was estimated to be ~46.25%, and this estimate removes the air volume from the volume of Si NW probed by the beam; the NWs are not internally mesoporous and thus the porosity in Eq. 11 is not related to porosity that may influence lattice conductivity. The thermal conductivity recalculated using this porosity reduces to 1.975 W/mK and of the same magnitude found experimentally for rough chemically etched Si NWs.

Conclusions

We proposed that the high-frequency roughness often discussed in recent analyses of spectra roughness contribution to phonon scattering and thermal conductivity reduction may be influenced by analysis of TEM images with multiple features observed (and added) in projection (so that the roughness frequency is misrepresentative). Scaling law for roughness and correlation length may need to consider additional substructure within the roughness. Second, the nanostructure of low rms roughness comprises significant nanocrystal density and grain boundaries that will confine phonons and induced significantly more grain and surface boundary scattering, and thus information has not been considered for certain roughness frequencies that have a limited effect on thermal conductivity suppression. Our results agree with the growing consensus that surface roughness and the spectrum of roughness wavelengths a priori may not be entirely responsible for the two order of magnitude suppression in thermal conductivity observed in many rough NW studies, and that the nature of the nanocrystalline feature within the roughness contribute to the overall scattering mechanisms. This study is important for providing information on the nature of the roughness and its effect on phonon transport within Si NWs. The nanostructure of the roughness features and evidence of multiphonon processes required to explain optical phonon mode shifts and asymmetric broadening with increasing temperature, may prove to be useful in explaining the uniquely suppressed thermal conductivities observed in Si NWs that are not coherent nor smooth. Estimates of thermal conductivity from Raman scattering confirms values similar to those reported well below the Casimir limit. Understanding what controls phonon transport in this important class of thermoelectric materials may prove useful for engineering their structure to optimize phonon scattering without largely affecting electronic conductivity or conduction states by dopants, defects of high grain boundary density.

Acknowledgments

C.G. acknowledges the support of the Irish Research Council under award RS/2011/797. This work was also supported by Science Foundation Ireland (SFI) under the National Access Programme (NAP 417), and through SFI Technology Innovation and Development Awards 2015 under contract 15/TIDA/2893.

References

1. A. I. Boukai, Y. Bunimovich, J. Tahir-Kheli, J.-K. Yu, W. A. Goddard Iii, and J. R. Heath, *Nature*, **451**, 168 (2008).
2. A. I. Hochbaum, R. K. Chen, R. D. Delgado, W. J. Liang, E. C. Garnett, M. Najarian, A. Majumdar, and P. D. Yang, *Nature*, **451**, 163 (2008).
3. J. Lim, K. Hippalgaonkar, S. C. Andrews, A. Majumdar, and P. Yang, *Nano Lett.*, **12**, 2475 (2012).
4. C. Dames and G. Chen, in *Thermoelectrics Handbook: Macro to Nano*, D. M. Rowe Editor, CRC (2006).
5. W. Kim, J. Zide, A. Gossard, D. Klenov, S. Stemmer, A. Shakouri, and A. Majumdar, *Phys. Rev. Lett.*, **96**, 045901 (2006).
6. C. Chiritescu, D. G. Cahill, N. Nguyen, D. Johnson, A. Bodapati, P. Keblinski, and P. Zschack, *Science*, **315**, 351 (2007).
7. T. C. Harman, P. J. Taylor, M. P. Walsh, and B. E. LaForge, *Science*, **297**, 2229 (2002).
8. R. Venkatasubramanian, E. Siivola, T. Colpitts, and B. O'Quinn, *Nature*, **413**, 597 (2001).
9. D. G. Cahill, M. Katiyar, and J. R. Abelson, *Philos Mag. B*, **71**, 677 (1995).
10. H. S. Yang, D. G. Cahill, X. Liu, J. L. Feldman, R. S. Crandall, B. A. Sperling, and J. R. Abelson, *Phys. Rev. B*, **81**, 104203 (2010).
11. G. J. Snyder and E. S. Toberer, *Nat. Mater.*, **7**, 105 (2008).
12. C. B. Vining, *Nat. Mater.*, **8**, 83 (2009).
13. L. Weber and E. Gmelin, *Appl. Phys. A*, **53**, 136 (1991).
14. H. B. G. Casimir, *Physica*, **5**, 495 (1938).
15. P. Martin, Z. Aksamija, E. Pop, and U. Ravaioli, *Phys. Rev. Lett.* , **102**, 125503 (2009).
16. J. Sadhu and S. Sinha, *Phys. Rev. B* **84**, 115450 (2011).
17. J. Carrete, L. J. Gallego, L. M. Varela, and N. Mingo, *Phys. Rev. B*, **84**, 075403 (2011).
18. F. X. Alvarez, D. Jou, and A. Sellitto, *J. Heat Transfer*, **133**, 022402 (2011).
19. L. Liu and X. Chen, *J. Appl. Phys.*, **107**, 033501 (2010).
20. W. McSweeney, C. Glynn, H. Geaney, G. Collins, J. D. Holmes, and C. O'Dwyer, *Semicond. Sci. Technol.*, **31**, 014003 (2016).
21. R.-p. Wang, G.-w. Zhou, Y.-l. Liu, S.-h. Pan, H.-z. Zhang, D.-p. Yu, and Z. Zhang, *Phys. Rev. B*, **61**, 16827 (2000).
22. G. Viera, S. Huet, and L. Boufendi, *J. Appl. Phys.*, **90**, 4175 (2001).
23. M. G. Ghossoub, K. V. Valavala, M. Seong, B. Azeredo, K. Hsu, J. S. Sadhu, P. K. Singh, and S. Sinha, *Nano Lett.*, **13**, 1564 (2013).
24. W. McSweeney, O. Lotty, N. Mogili, C. Glynn, H. Geaney, D. Tanner, J. Holmes, and C. O'Dwyer, *J. Appl. Phys.*, **114**, 034309 (2013).
25. W. McSweeney, H. Geaney, and C. O'Dwyer, *Nano Res.*, **8**, 1395 (2015).
26. K. Balasundaram, J. S. Sadhu, J. C. Shin, B. Azeredo, D. Chanda, M. Malik, K. Hsu, J. A. Rogers, P. Ferreira, S. Sinha, and X. Li, *Nanotechnology*, **23**, 305304 (2012).
27. N. Geyer, B. Fuhrmann, Z. Huang, J. de Boor, H. S. Leipner, and P. Werner, *J. Phys. Chem. C*, **116**, 13446 (2012).
28. D. H. Lee, Y. Kim, G. S. Doerk, I. Laboriante, and R. Maboudian, *J. Mater. Chem.*, **21**, 10359 (2011).
29. D. G. Cahill, P. V. Braun, G. Chen, D. R. Clarke, S. Fan, K. E. Goodson, P. Keblinski, W. P. King, G. D. Mahan, A. Majumdar, H. J. Maris, S. R. Phillpot, E. Pop, and L. Shi, *Appl. Phys. Rev.*, **1**, 011305 (2014).
30. M. Balkanski, R. F. Wallis, and E. Haro, *Phys. Rev. B*, **28**, 1928 (1983).
31. J. Zi, H. Büscher, C. Falter, W. Ludwig, K. Zhang, and X. Xie, *Appl. Phys. Lett.*, **69**, 200 (1996).
32. K. Adu, Q. Xiong, H. Gutierrez, G. Chen, and P. Eklund, *Appl. Phys. A*, **85**, 287 (2006).
33. B. Li, D. Yu, and S. L. Zhang, *Phys. Rev. B*, **59**, 1645 (1999).
34. S. Piscanec, M. Cantoro, A. Ferrari, J. Zapien, Y. Lifshitz, S. Lee, S. Hofmann, and J. Robertson, *Phys. Rev. B*, **68**, 241312 (2003).
35. I. Ponomareva, D. Srivastava, and M. Menon, *Nano Lett.*, **7**, 1155 (2007).
36. Y. Chen, B. Peng, and B. Wang, *J. Phys. Chem. C*, **1111**, 5855 (2007).
37. P. Mishra and K. P. Jain, *Phys. Rev. B*, **62**, 14790 (2000).
38. Q. Hao, *J. Appl. Phys.*, **111**, 014307 (2012).
39. J. P. Feser, J. S. Sadhu, B. P. Azeredo, K. H. Hsu, J. Ma, J. Kim, M. Seong, N. X. Fang, X. Li, P. M. Ferreira, S. Sinha, and D. G. Cahill, *J. Appl. Phys.*, **112**, 114306 (2012).
40. C. O'Dwyer, W. McSweeney, and G. Collins, *ECS J. Solid State Sci. Technol.*, **5**, R3059 (2016).
41. Y. He and G. Galli, *Phys. Rev. Lett.*, **108**, 215901 (2012).
42. I. H. Campbell and P. M. Fauchet, *Solid State Commun.*, **58**, 739 (1986).
43. T. Feng and X. Ruan, *Phys. Rev. B*, **93**, 045202 (2016).
44. S. Périchon, V. Lysenko, B. Remaki, D. Barbier, and B. Champagnon, *J. Appl. Phys.*, **86**, 4700 (1999).
45. L. Hu and G. Chen, *Nano Lett.*, **7**, 3249 (2007).